DØ Note # 2149

Recent QCD results from the Tevatron $\bar{p}p$ collider at $\sqrt{s} = 1.8$ TeV [1]

Jaehoon Yu[2]
Department of Physics & Astronomy
University of Rochester
Rochester, NY 14627, USA

Abstract: Recent results of QCD studies from the CDF and DØ experiments at the Tevatron $\bar{p}p$ collider at Fermilab are presented. The inclusive jet cross section, the internal structure of jets, di-jet angular distributions, di-jet triple differential cross sections, and properties of multi-jet final states are studied and compared with NLO QCD predictions. The comparisons show good agreement between theoretical predictions and the experimental data in general. Some systematic disagreement between LO predictions and the data are observed in di-jet triple differential cross sections. Results of a rapidity gap study are also presented together with an upper limit on the gap fraction. In addition, the inclusive photon cross section and the di-photon cross sections are presented and compared with NLO QCD predictions.

1 Introduction

Quantum Chromodynamics (QCD) is the quantum field theory describing the dynamics of the strong interactions. In QCD, strong interaction is interpreted as the interaction between color charged partons [1] and the forces in the strong interactions are mediated by colored field quanta, gluons [2]. Confinement and asymptotic freedom [1] are two of its main characteristics. Confinement explains why partons only exist in bound colorless states. Asymptotic freedom enables perturbative techniques to be used to calculate predictions for large momentum transfer processes. One of the first predictions of QCD was the existence of the three jet events in e^+e^- collisions and the experimental observation of such events [3] was one of the conerstones of verifying the QCD prediction experimentally. Since then there have been enormous improvements in QCD from both experiment and theory.

QCD predictions of cross sections in high energy $\bar{p}p$ scattering consist of two main ingredients. One is the parton distribution functions (PDF) which describe the distributions

---

[1] Talk given at the 22nd INS symposium, Tokyo, Japan, March 1994.

[2] Author supported by the National Science Foundation of the US government.

of fractional momenta of the partons making up protons and antiprotons. The other is the hard scattering cross section which represents the probability of occurrence of certain process from a particular set of initial state parton configurations. From many deep inelastic scattering experiments, parton distribution functions are well determined in a wide range of intermediate fractional momenta. In addition, cross sections for many processes from hard interactions are predicted by perturbative QCD (PQCD) in both leading order (LO) and next-to-leading order (NLO). The NLO calculations provide more realistic algorithms for jet definitions and enable more reliable comparisons between theoretical predictions and experimental measurements. These improvements in theory provide more stable and reliable predictions on many physically measurable quantities.

Experimentally, the Tevatron collider at Fermilab has been operating since 1987. With the newly comissioned D0 detector at one of its collision points and the upgraded CDF (Collider Detector at Fermilab) detector, the contribution of the Fermilab Tevatron collider to QCD physics is measurable. Descriptions of both the CDF [4] and D0 [5] detectors can be found elsewhere. The total integrated luminosity accumulated during 1992-1993 collider run are approximately $21pb^{-1}$ and $16pb^{-1}$ for CDF and D0 experiment, respectively. The data samples of jet and photon final states consists of several million events.

Generally, in hadron colliders jet algorithms define a cluster using a fixed cone in $\eta - \phi$ space where η is pseudorapidity ($\eta = -ln[tan\theta/2]$) and ϕ is the azimuthal angle. The radius of the jet cone is defined in $\eta - \phi$ space as $\Delta R = \sqrt{(\Delta\eta)^2 + (\Delta\phi)^2}$. In this review, most jets are defined with $\Delta R = 0.7$ except a few cases with $\Delta R = 1.0$. In all the analyses involving jets, the energies of jets are corrected for detector response. These corrections range between 15% to 30% depending on the transverse energy, E_T, and η of the jet. The uncertainties of the jet energy scale corrections are on the order of 4% - 5%. These errors are small, but it can be seen that the cross sections which typically fall like E_T^{-n} with $n = 5 \sim 6$ have errors on the order of 20 to 30%.

Although, there are many other final states that can be used for QCD study, such as heavy quarks and heavy vector bosons (W and Z), this review summarizes results only from the analyses using events with jet and direct photon final states. The results presented in this review are mostly based on the analyses from the data taken during 1992-1993 Tevatron collider run from both experiments.

2 Inclusive jet E_T spectrum

Measurement of the inclusive jet E_T cross section provides a simultaneous test of both PDF's and hard scattering cross sections, because the cross section spans many orders of magnitude in a wide range of E_T. Now that the NLO PQCD prediction, $O(\alpha_s^3)$, exists a more stringent test of the theoretical prediction is possible. In addition, deviations of the spectrum from the QCD predictions can also provide evidence of quark substructure. Experimentally, with the given statistics, both experiments at the Tevatron collider measured the spectrum to approximately 450 GeV in E_T in the central rapidity region.

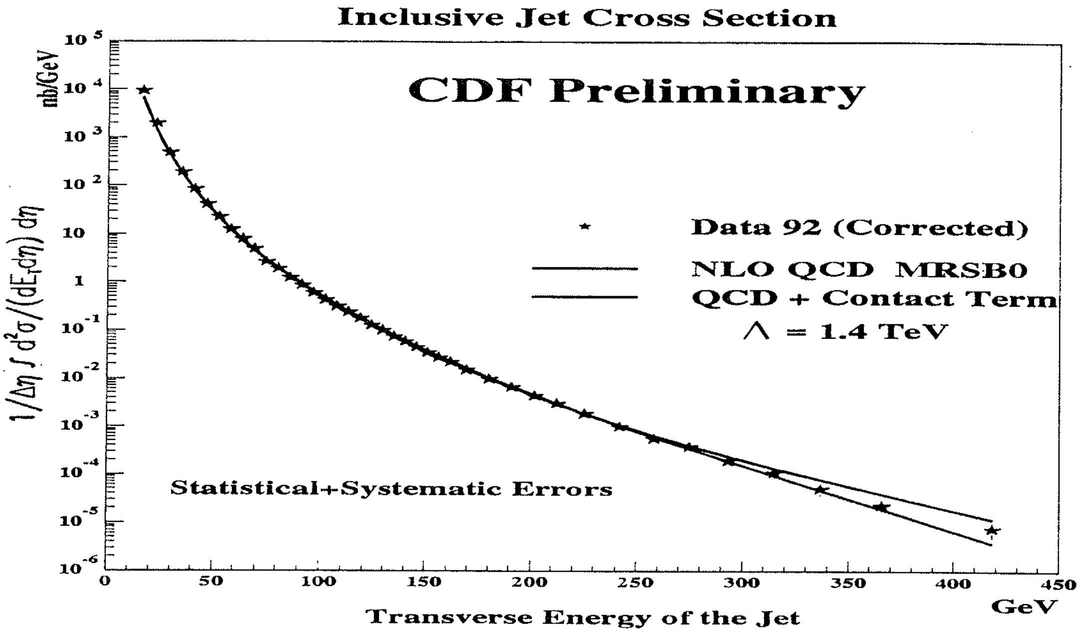

Figure 1: Jet inclusive differential cross section from CDF experiment

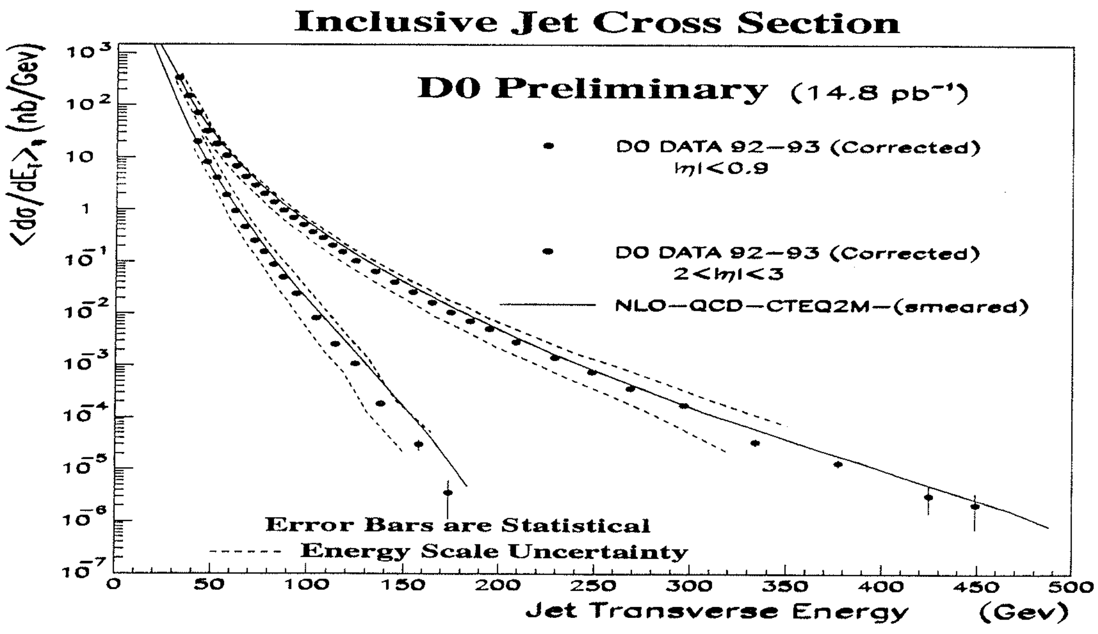

Figure 2: Jet inclusive differential cross section from DØ experiment

Figure 1 shows the spectrum in the central rapidity region ($|\eta|<0.7$) for CDF. Shown on the vertical axis is the inclusive cross section averaged over the η interval. E_T of the jets are corrected by the measured CDF jet energy response. The data points on the plot are corrected for the detector jet energy resolution. The lower solid line in Fig. 1 is NLO QCD prediction [6] using $MRSB^0$ parton distribution functions. As can be seen in Fig. 1, the theoretical prediction agrees remarkably well throughout the entire range of E_T spectrum over ten orders of magnitude in the cross section. The upper solid line is the QCD prediction with a contact term which describes the energy scale at which quark substructure can be expected to manifest itself, Λ_c=1.4TeV. Based on the comparisons of the experimental data with the theoretical prediction, CDF has set a new lower limit on the scale of quark substructure with $\Lambda_c >$1.45TeV at 95% confidence level.

Figure 2 shows the cross sections both in the central rapidity ($|\eta|<0.9$) and forward rapidity region ($2.0<|\eta|<3.0$) from the DØ experiment. The upper set of data points in Fig. 2 indicates the spectrum in the central region ($|\eta|< 0.9$) and the lower set illustrates the spectrum in the forward region ($2.0 <|\eta|< 3.0$). The E_T of the jets in the plot are corrected by the measured jet energy response of the DØ detector. The dotted lines around the data points indicate the current experimental systematic uncertainty from the jet energy correction. The solid lines in the plot indicate NLO QCD predictions with CTEQ2M parton distribution functions for both the central and the forward rapidity regions. The theoretical predictions are smeared by the measured DØ jet energy resolution to compare directly with experimental data. Just like the CDF results, the theoretical prediction in the central region is in good agreement with the experimentally measured data. The new information is in the forward rapidity region ($2.0 <|\eta|< 3.0$) as shown in Fig. 2. Previously only one measurement exists from the UA2 experiment where the differential cross section is measured out to pseudorapidity of two [7]. The comparison of the cross section from the UA2 with LO QCD prediction showed disagreement in the forward region. However, the new results from DØ experiment show good agreement when compared with NLO prediction.

3 Energy flow within a jet

As discussed in the previous section, the inclusive jet E_T cross section can be described successfully by NLO PQCD where the predictions are done at the parton level. This exercise is the evidence of parton hadron duality theorem [8] which states that parton level and hadron level distributions in hard processes are identical. In other words, even if the dynamics of the colorless final states (hadrons) involving low momentum transfer cannot be predicted by PQCD, the global picture of the final state hadronic clusters in hard processes is in principle calculable from PQCD at the parton level. Since we have seen that inclusive cross section of jets can be described by PQCD successfully, we can ask whether the detailed structure of the jet can also be described by the NLO PQCD prediction. The internal structure of jets is expected to be governed more by the dynamics of the low momentum transfer processes than by the high momentum transfer processes which preserve the perturbative nature. In LO $2 \rightarrow 2$ process, jets are represented solely by single partons so that the jets cannot have any structure. In NLO, however, there are contributions from $2 \rightarrow 2$ processes as well as

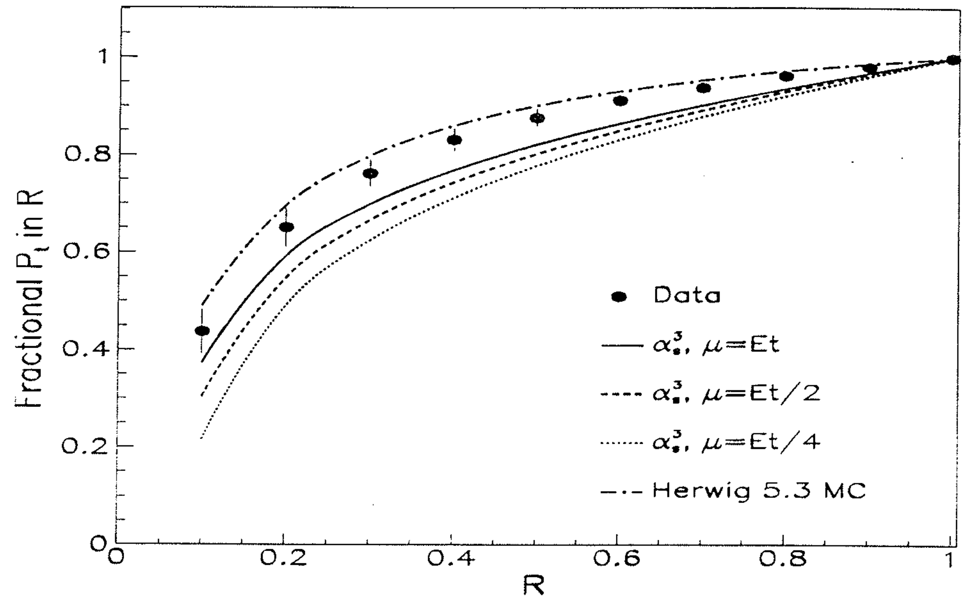

Figure 3: Energy flow within jets from CDF [9].

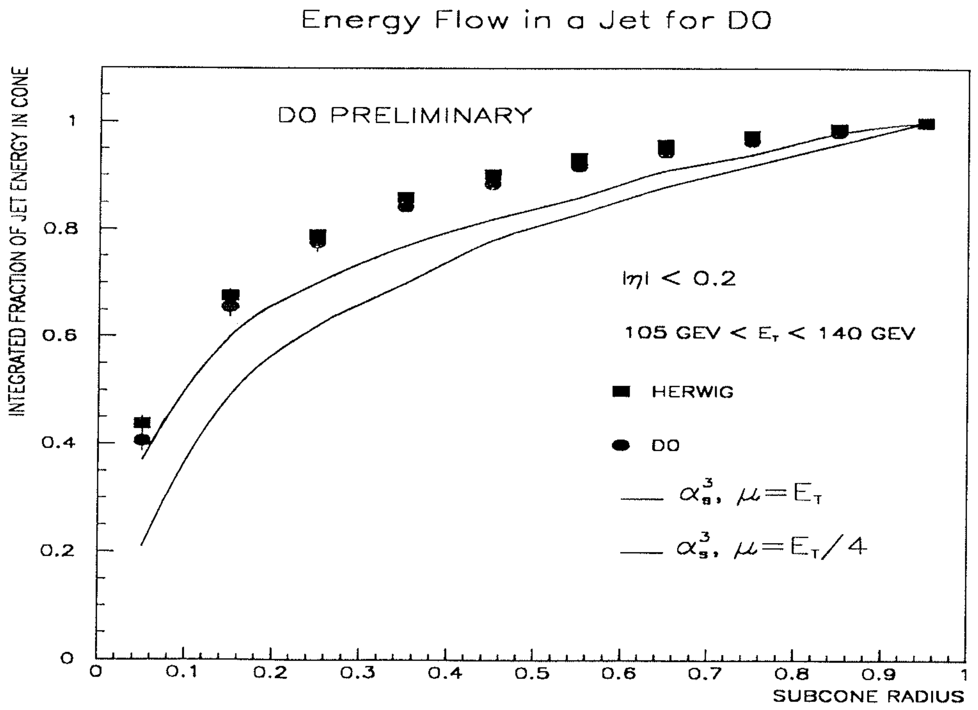

Figure 4: Energy flow within jets from DØ

$2 \rightarrow 3$ processes. The directions and the energies of jets in NLO then are represented not only by single partons but also by the vector sum of two partons within the cone which defines a jet. Therefore, the NLO PQCD prediction can provide some information on the internal structure of jets.

To test the PQCD prediction for this detailed nature of jets, both the CDF and DØ experiments performed studies on the internal energy flow of jets. The methods of these analyses are to normalize the energy in subcones of various sizes to the total energy of the jet inside the cone of size 1.0 in $\eta - \phi$ space. The variation of the fractional energy as a function of subcone radius is a measure of the internal structure of the jet.

The two experiments used slightly different methods to compare the data with the theoretical predictions. The CDF experiment, utilizing their central magnetic field, defines the momentum of a jet from the sum of the charged track momenta in the jet subcone. The fractional momentum is then defined as:

$$f(\Delta R = r) = \frac{\Sigma \vec{P_T}(\Delta R = r)}{\Sigma \vec{P_T}(\Delta R = 1.0)} \tag{1}$$

The DØ experiment uses the E_T in the calorimeter within subcones of varying size to measure the energy flow. As this method includes neutral particles, it minimizes uncertainties due to just measuring the momentum of the charged particles within the jet despite the intrinsic calorimeter energy resolution. The definition of the fractional E_T is:

$$f(\Delta R = r) = \frac{\Sigma E_T(\Delta R = r)}{\Sigma E_T(\Delta R = 1.0)} \tag{2}$$

Figures 3 and 4 show the measured distributions of the fractional momenta as a function of subcone size for CDF and DØ for 100 GeV jets. The jets are limited to the central region ($|\eta| < 0.7$) to preserve the maximum efficiency in momentum measurements in the central magnetic field for CDF analysis and at the same time to keep the transverse momentum and the energy the same. The DØ data points also includes only the central jet for a comparison of the data from the two experiments. The solid circles in both figures represent experimental data. The dot-and-dashed line in Fig. 3 and the solid squares in Fig. 4 indicate the prediction from parton shower Monte Carlo (HERWIG) [10]. HERWIG is a Monte Carlo generator based on a LO QCD calculations and includes various radiations of partons. The other lines on the figures are the NLO PQCD predictions with various renormalization scale (μ_R) [11].

One can infer from both figures that a 100 GeV jet has more than 40% of its energy contained within the core of size 0.1. The profile of the fractional energy is properly described by HERWIG as can be seen from both plots. Although the NLO QCD can predict qualitatively the same structure, it still suffers from large dependence to the renormalization scale (μ_R). This is due to the fact that the NLO is the first order in which the internal structure of a jet can be described. Thus the large dependence of the prediction to the renormalization scale, μ_R, in describing the jet internal structure is not surprising. From

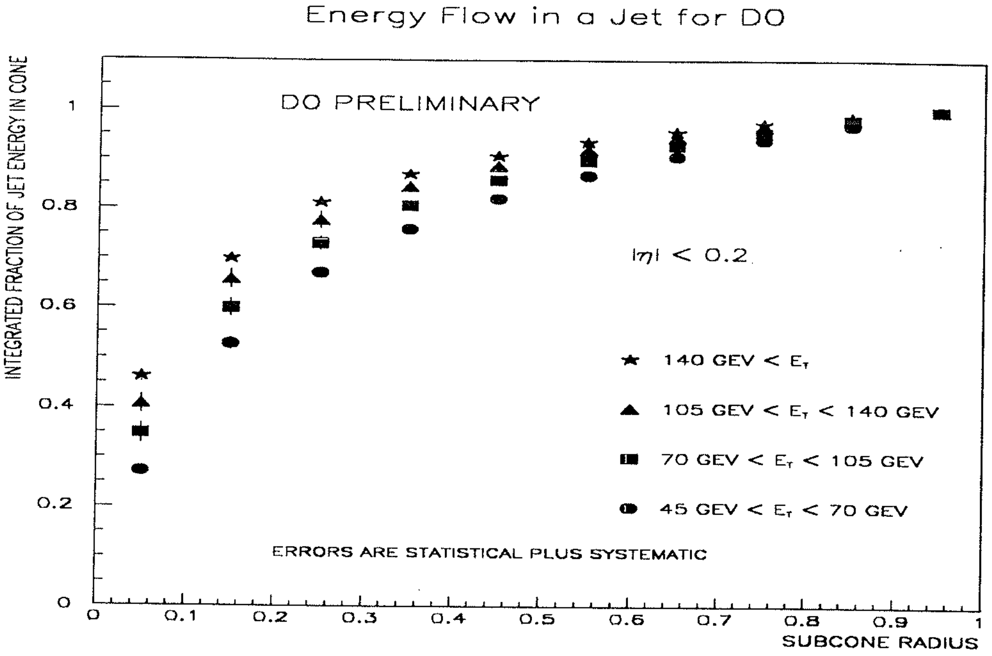

Figure 5: E_T dependence of the jet profile from DØ

these measurements, it can be concluded that it is necessary to have more than just the NLO parton level predictions to describe the detailed structure of jets.

The energy dependence of the internal structure of jets has also been measured. Figure 5 demonstrates the E_T dependence of the energy profile of the jet from DØ's fractional E_T measurements. The plot shows the jet energy profile for four different jet energy intervals. One can observe from the plot that as the jet energy increases the profile of the jet gets narrower. The jets with energy between 45 and 70 GeV have approximately 25% of their energy in the core cone with size 0.1 whereas the jets with energy greater than 140GeV have more than 45% of their energy in the core cone. The same behavior was observed from CDF results in reference [12]. Parton shower Monte Carlo predictions have qualitatively shown the same behavior as the data.

To carry out this study one step further, one would like to distinguish quark initiated jets from gluon initiated jets. This study has been performed by the OPAL collaboration at LEP recently using three jet final states from hadronic decay of Z^0 bosons to ensure a gluon jet in the final state [13]. Since Z^0 bosons only couple a quark and an antiquark, the third jet can only come from a radiation of one of the quark jets in the final state. Hence the third jet is likely to be a gluon jet and the three jet events include enriched sample of of gluon initiated jets. The study showed that the gluon initiated jets have a broader profile than quark initiated jets. Special techniques are needed to study this at $\bar{p}p$ colliders. A proposed method is to use semileptonic decays of heavy quarks (b or c quarks). Since decays of these heavy quarks result soft leptons adjacent to the jets, tagging these soft leptons and studying the internal structure of these adjacent jets will provide a means of selecting out quark initiated jets. This method is currently under investigation by both experiments at the Tevatron collider.

4 Two jet angular distributions

The differential distribution, $d^3\sigma/dE_T d\eta^* d\eta_{boost}$, can be used to describe the inclusive two jet final state. This differential distribution has a direct relationship with the angular distribution of the two jet system in the center-of-mass system (CMS) as follows:

$$\eta_{Boost} = \frac{\eta_1 + \eta_2}{2}, \quad \eta^* = \frac{\eta_1 - \eta_2}{2}$$
$$cos\theta^* = tanh\ \eta^*, \quad M_{jj} = 2E_T cosh\ \eta^* \tag{3}$$

The superscript * refers to the CMS, η_1 and η_2 are pseudorapidity of the two leading E_T jets in the lab frame and θ^* is the polar angle of the leading E_T jet in the CMS relative to the incoming parton direction. Based on the relationship in Eq. 3, the angular distribution of the jet in the CMS can be directly measured as a function of $cos\theta^*$. This angular distribution at Tevatron energies is dominated by t-channel vector gluon exchange. Therefore, the distribution follows Rutherford scattering characteristics of spin 1 particle exchange, $dN/dcos\theta^* \approx (1 - cos\theta^*)^{-2}$. Figure 6 shows the measured angular distribution of leading E_T jet from the DØ experiment with the leading two jet invariant mass, $175 < M_{jj} < 350$ GeV/c^2. Shown on the vertical axis are the number of events normalized to the bin size. The solid circles represent experimental data corrected for the energy and position resolution of the detector. The solid line represents NLO QCD prediction and the dotted line indicates the LO prediction. The comparisons demonstrate good agreement between data and both the LO and NLO predictions. Since the distribution varies very rapidly as $cos\theta^*$ increases due to the pole at $cos\theta^* = 1$, however, this distribution is not suitable for a detailed comparison between theory and experiment. For this reason a variable χ, defined in Eq. 4, which transforms a $(1 - cos\theta^*)^{-2}$ type distribution into a flat distribution is used to study the angular distribution. The relationships between the variables used to describe the di-jet system are as follows:

$$\chi = e^{2|\eta^*|} = \frac{(1 + cos\theta^*)}{(1 - cos\theta^*)} \tag{4}$$

By changing variables based on Eq. 3, one can describe the two jet final state by the cross section $d^3\sigma/dM_{jj}d\eta^* d\eta_{Boost}$. This differential cross section depends on the parton distribution functions and the hard scattering cross section. One can remove most of the effect of parton distribution function by integrating this cross section over wide ranges of the M_{jj} and η_{Boost} space, because the M_{jj} and η_{Boost} are determined by the momenta of the initial state partons. Using Eq. 4, the resulting cross section after the integration can then turn to a normalized distribution $N^{-1}dN/d\chi$ which is typically refered to as the di-jet angular distribution. Figure 7 shows the $N^{-1}dN/d\chi$ distributions for three different di-jet invariant mass ranges from CDF. The open circles indicate data points from experimental measurement, the solid lines represent NLO QCD predictions, and the dashed lines illustrates LO

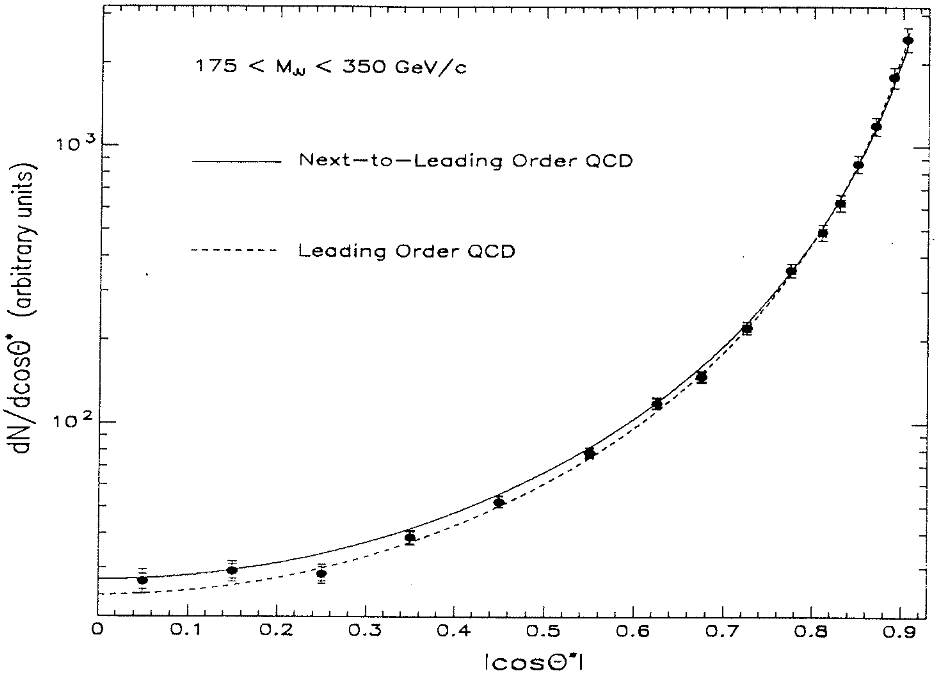

Figure 6: cosθ^* distribution from DØ

QCD predictions. From the upper most plot down, the plots show the distributions with 240 < M_{jj} <475 GeV/c^2, 475 < M_{jj} < 550 GeV/c^2, and 550GeV/c^2< M_{jj}. Both NLO and LO theoretical predictions show good agreement within the experimental error in all three invariant mass ranges. The maximum value of χ on the plot is approximately $\chi = 25$ which corresponds to $cos\theta^* \sim 0.67$.

Figure 8 shows the same distributions for the DØ experiment. From the upper most plot the kinematic range of the distributions are 175 < M_{jj} < 350GeV with η_{Boost} < 2.0, 350 < M_{jj} < 450GeV/c^2 with η_{Boost} < 1.5, and 450GeV/c^2< M_{jj} with η_{Boost} < 0.7. The ranges of M_{jj} and η_{Boost} were chosen to keep the detector acceptance as uniform as possible. The experimental data have been corrected for trigger efficiencies, detector acceptance, and angular resolution smearing. These corrections are typically less than 10% for $\chi < 25$ and can be as large as 30% at $\chi \approx 200$. The uncertainty from these corrections and the jet energy scale correction is reflected in the systematic error on the data points. The acceptance and angular resolution corrections are determined using the Papageno Monte Carlo [14]. In the upper most plot, the experimental results are compared with three theoretical predictions. The dotted line indicates the LO QCD scaling prediction where parton distributions and α_s are evaluated at a fixed scale. This corresponds to Rutherford scattering and clearly disagrees with data throughout the entire range of the quantity χ. The sharp rise of the distribution at small χ is due to the contribution from s-channel exchange. The dashed line indicates the LO prediction with α_s varying with renormalization scale $\mu_R = E_T/2$ using Duke and Owens parton distribution funtions set two [15]. (This variation of the value of α_s

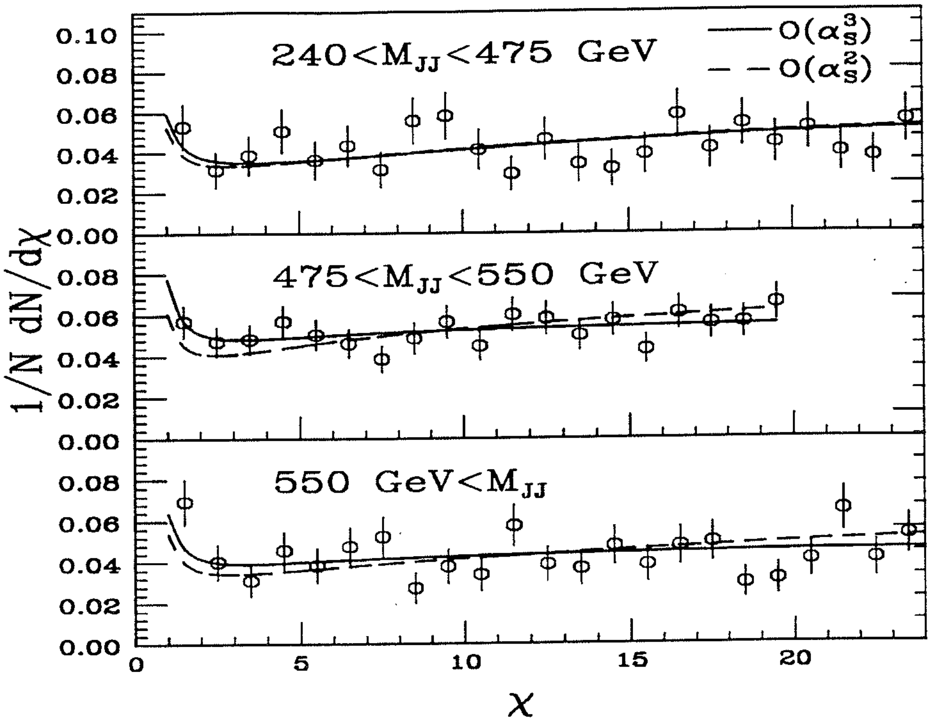

Figure 7: $1/\mathrm{N}dN/d\chi$ distributions with three different mass ranges from CDF [18].

with momentum transfer scale is typically called the running of α_s.) The running of α_s as a function of momentum transfer ensures the asymptotic freedom which is one of the basic premises of the perturbative QCD. Using the running α_s, the LO QCD prediction already shows better agreement with the data. Since the shape of the distribution is insensitive to the parton distributions, this drastic improvement is a direct evidence of the running α_s. The solid line represents the NLO QCD prediction [16]. Figure 8.b shows the distribution in $350 < M_{jj} < 450$GeV with $\eta_{Boost} < 1.5$. Here the NLO prediction shows better agreement with the data in the entire range of χ whereas the LO shows disagreement at the low and high values of χ. The Fig 8.c shows the same distribution for $M_{jj} > 450\ GeV/c^2$ and η_{Boost} <0.7. The χ coverage in this plot extends to approximately $\chi = 250$ which corresponds to $cos\theta^* \sim 0.94$. This extension of the χ coverage is possible due to the large rapidity coverage of the detector. From Eq. 3 and 4, requiring M_{jj} to be large and keeping E_T small results the large η^* and hence the χ. In addition, large rapidity coverage of the detector enables detecting jets with large rapidity and at the same time requiring η_{boost} small keeps the detector acceptance uniform. This extension in χ is approximately ten times bigger the χ range than the previously available measurements [18]. Although the data have large error the agreement between experimental data and QCD prediction still persists.

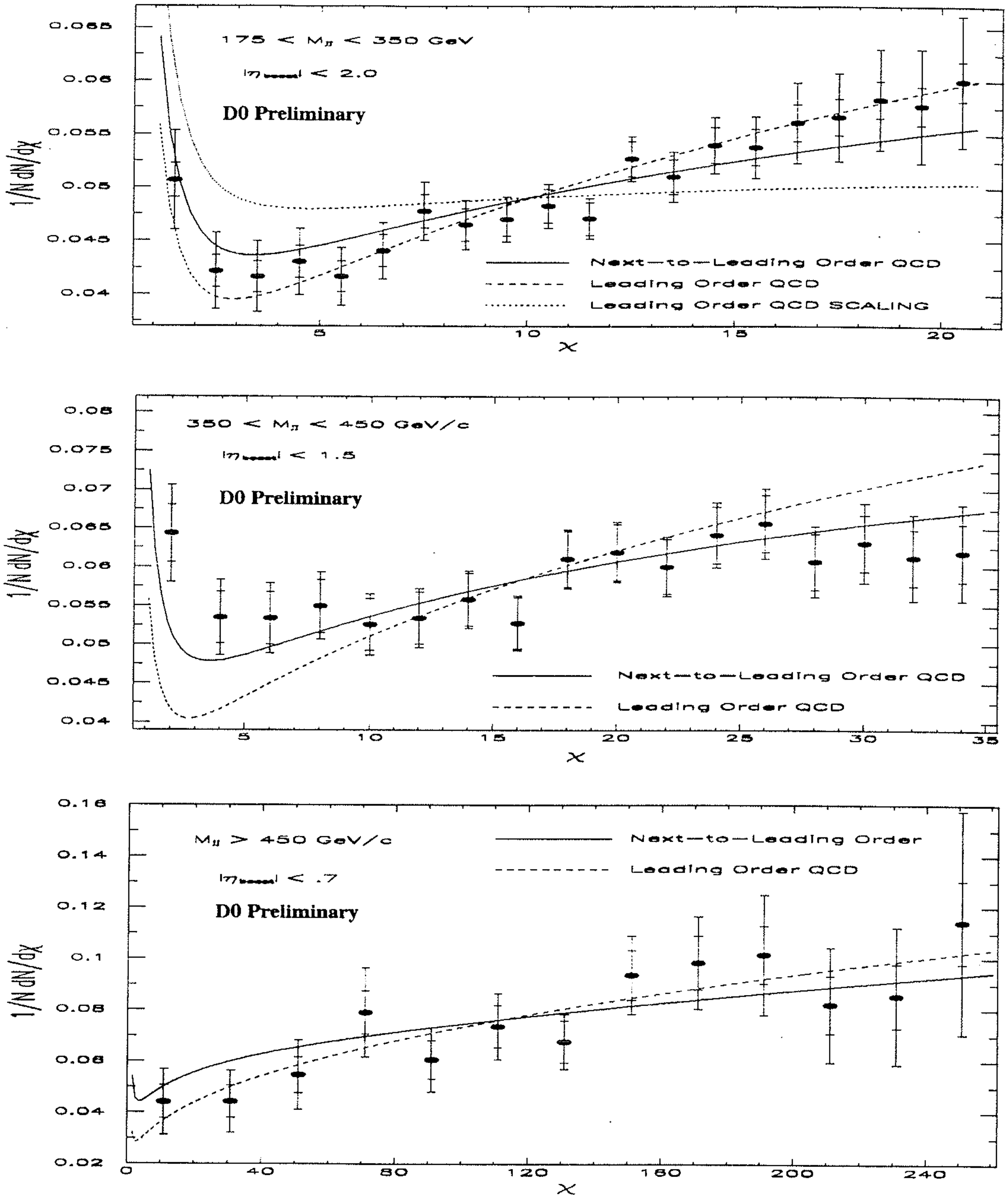

Figure 8: $1/NdN/d\chi$ distributions with three different mass ranges from DØ

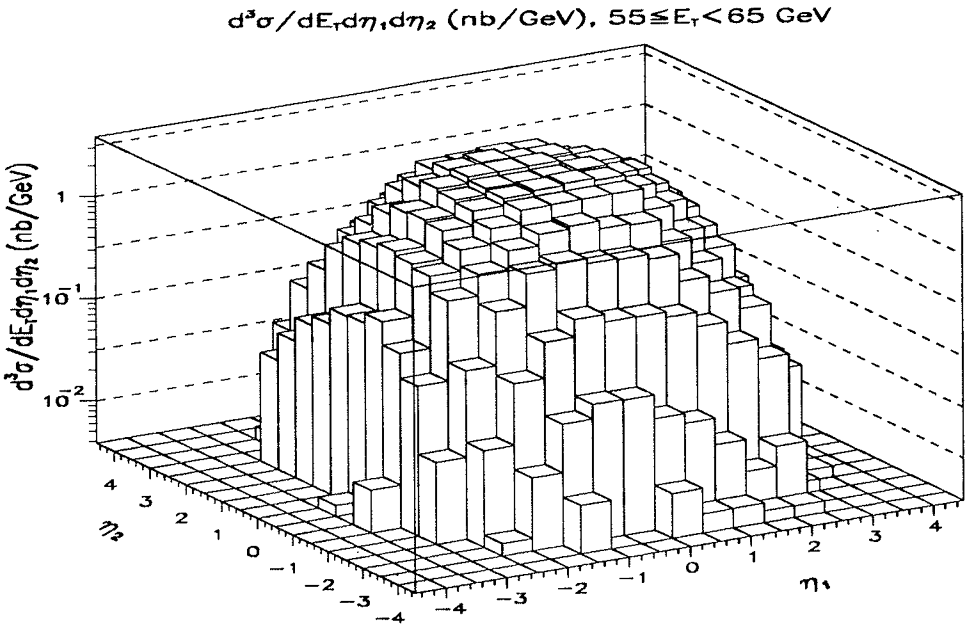

Figure 9: $d^3\sigma/dE_T^1d\eta_1d\eta_2$ vs η_1 and η_2 from DØ

5 Di-jet triple differential cross section

The comparison shown in section 4 implies that LO and NLO predictions describe the shape of the di-jet angular distribution very well. The shape of the angular distribution is predominantly determined by the hard scattering cross section. Therefore, the good agreement between the experimental data and theoretical predictions implies that the matrix element calculations are correct within the experimental uncertainty. We now then turn our attention to extracting information on the parton distributions from di-jet events.

The rapidity and E_T of the final state jets have a direct relationship with the initial state parton momentum fractions, x_1 and x_2 as follows:

$$x_1 = E_T(e^{\eta_1} + e^{\eta_2})/\sqrt{s}, \qquad x_2 = E_T(e^{-\eta_1} + e^{-\eta_2})/\sqrt{s} \tag{5}$$

where η_1 and η_2 are the pseudorapidity of the final state jets under the assumption that the jets are massless objects. Based on Eq. 5, one can explore different ranges of fractional momenta of the initial state partons depending on the rapidity configuration of the jets in the final state at fixed E_T. By measuring the differential cross section, $d\sigma/dE_Td\eta_1d\eta_2$, as a function of leading jet E_T, leading jet rapidity (η_1), and the second leading jet rapidity (η_2), one can extract the information of the parton distribution.

Figure 9 shows differential cross section, $d^3\sigma/dE_T^1d\eta_1d\eta_2$, as a function of η_1 and η_2 for E_T of the leading jet fixed between 55 and 65GeV. One can observe the rapidity plateau at the center of the distributions as expected based on inclusive η distributions of jets.

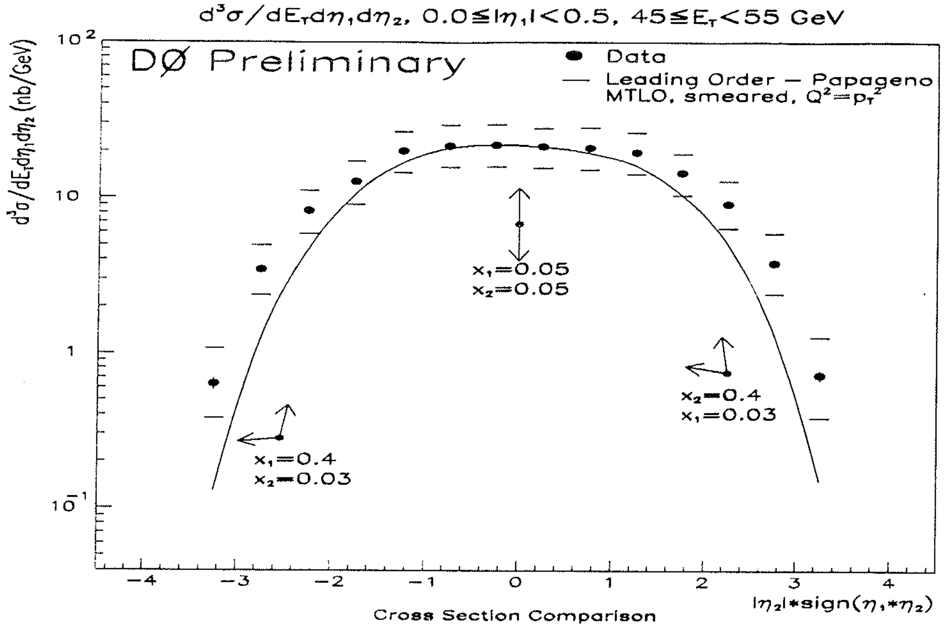

Figure 10: $d^3\sigma/dE_T^1 d\eta_1 d\eta_2$ vs η_1 and η_2 from DØ

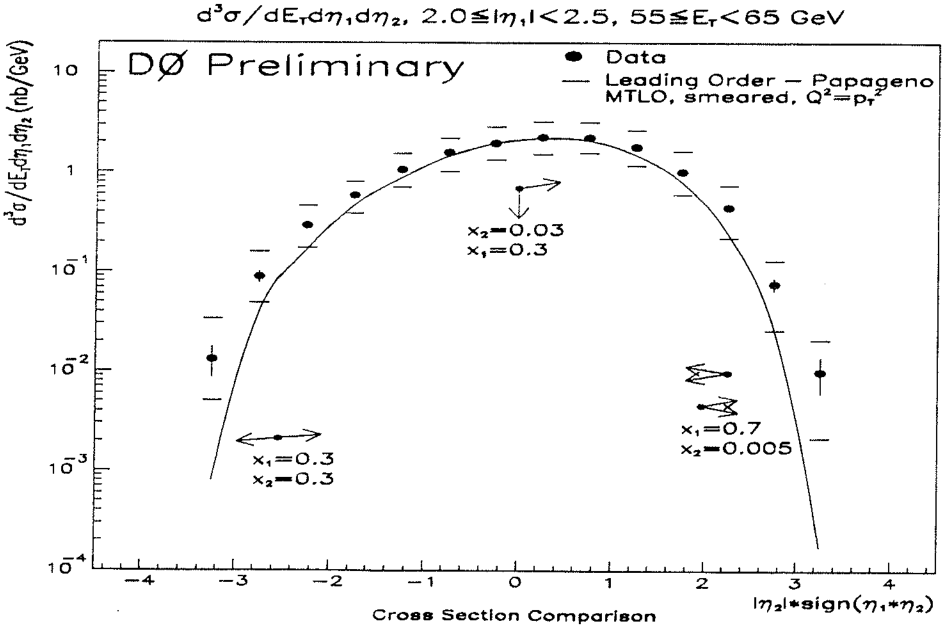

Figure 11: $d^3\sigma/dE_T^1 d\eta_1 d\eta_2$ vs η_1 and η_2 from DØ

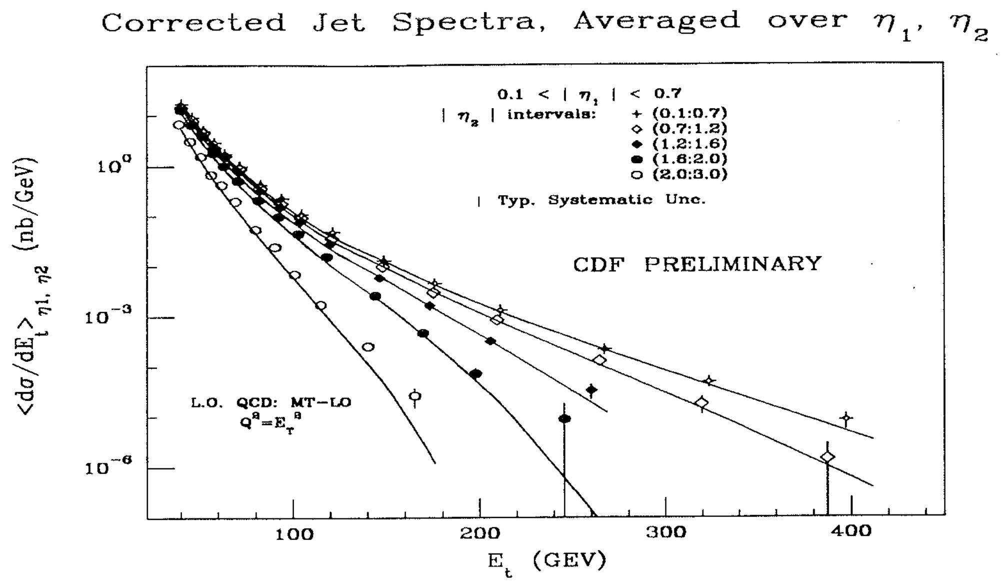

Corrected Jet Spectra, Averaged over η_1, η_2

Figure 12: Leading jet E_T spectrum for various rapidity regions of the second E_T jet from CDF

Since a visual comparison of the theoretical prediction and data is not so straight forward in this three dimensional plot, however, D0 choses to plot the cross section as a function of the quantity $| \eta_2 | sign(\eta_1 \cdot \eta_2)$. This particular quantity essentially distinguishes the two final state jets with the same signs of η from the jets with opposite signs of the η. Figures 10 and 11 show the cross sections as a function of the above quantity. Figure 10 shows the differential cross section as a function of $| \eta_2 |$ for $0 < | \eta_1 | < 0.5$ and the leading jet E_T, $45 < E_T < 55$ GeV. Figure 11 shows the same cross section for $2.0 < | \eta_1 | < 2.5$ and $55 < E_T < 65$ GeV. These E_T ranges are chosen to ensure the full efficiency of the D0 trigger. The solid circles on the figures indicate experimental data points, and the solid lines represent LO QCD prediction from Papageno Monte Carlo smeared with detector resolution using MT-LO [19] parton distribution functions with renormalization scale $\mu_R = P_T$. These theoretical predictions are normalized to the data point at 0.25 to compare the shape. The arrows and the number beneath them in the plots show the η configuration of the final state jets and x_1 and x_2 of the initial state partons, respectively. When η of the leading jet is fixed in the central rapidity region, the achievable initial state fractional momenta are in the intermediate range. However, when η of the leading jet is fixed in the high rapidity, the fractional momenta extends down to 0.005 as the second jet moves forward. These plots show gradual difference between the experimental measurement and theoretical predictions as one jet moves more forward. Generally the LO QCD prediction describes the shape of the distribution well when both jets stay in the central rapidity region. If one jet is at large rapidity, we expect large NLO corrections, hence NLO predictions are necessary before any quantitative conclusions can be drawn. Recently, the NLO QCD prediction has become available [20]. Comparisons of the NLO prediction and the experimental data with many different parton distribution functions are currently being pursued.

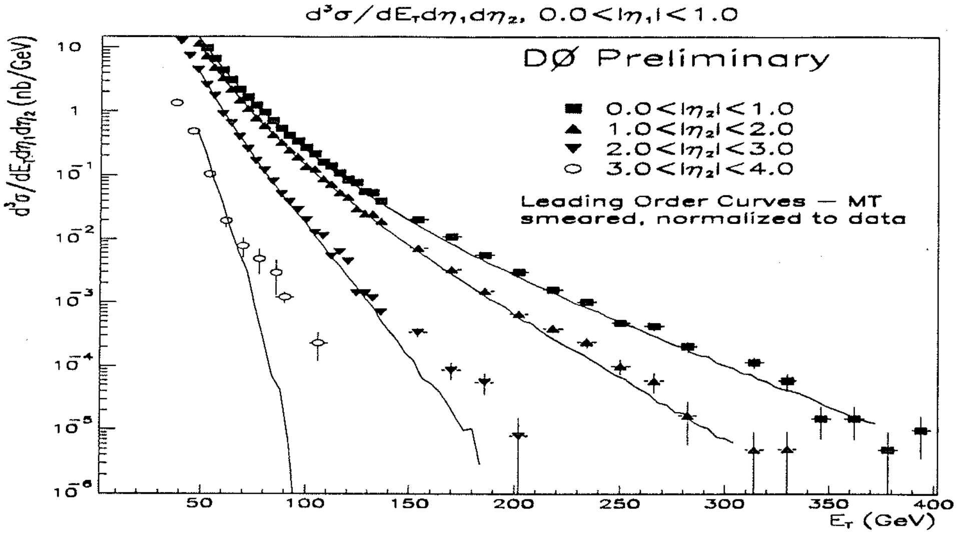

Figure 13: Leading jet E_T spectrum for various rapidity regions of the second E_T jet from DØ

Figures 12 and 13 show leading jet E_T spectrum for various ranges of η_2. Shown on the vertical axis is the differential cross section as a function of leading jet E_T for a fixed rapidity interval of the leading jet. Fig 12 shows the differential cross section for four different intervals of the second jet rapidity, η_2, with $0.1 <| \eta_1 |< 0.7$ from the CDF experiment. The various symbols indicate the experimental data in different intervals of η_2 and the solid lines indicate LO QCD predictions with MT-LO parton distribution functions. Figure 13 shows the same cross section measured in slightly different intervals of η_2 for the DØ experiment. Again various symbols represent experimental data and the solid lines indicate LO prediction using MT-LO parton distribution functions. In Fig. 12, experimental data are corrected for the detector effects. In Fig. 13, the theoretical predictions are smeared by the detector resolution and normalized to the data. As one can observe from the figures, the LO predictions are in good agreement when both jets are restricted to the central rapidity region where the two initial state fractional momenta are approximately in the same range. However, a systematic disagreement between data and LO theoretical predictions can be observed as the probing jet, second E_T jet, moves to higher rapidity. The LO prediction shows smaller cross section as a function of E_T for large η_2 and the difference between the prediction and the data becomes larger as the η_2 moves forward.

One of the possible causes of the discrepancy between experimental data and LO prediction is the kinematic limit of the jet E_T due to the constraint on the total available center of mass energy. Since in LO there are two and only two partons representing the energies and directions of the two jets in the final state, the E_T of the two partons must be balanced. However, kinematically allowed region of the jet E_T is limited by the center of mass energy through the relationship $E_T \leq (\sqrt{s}/2) \times sin\theta$, where θ is the polar angle of the jet from the beam direction. Therefore, the jets in the central rapidity can in principle have the E_T as large as $\sqrt{s}/2$ where as the jets in the forward rapidity at an angle θ can only have the maximum $E_T = (\sqrt{s}/2) \times sin\theta$. Hence, the LO theoretical prediction would soon reach the kinematic limit imposed on the jets due to the $sin\theta$ factor. On the other hand, in NLO there are either two or three partons in the final state forming jets. The two jets represented by two partons do not necessarily have to balance the E_T because there is another parton which did not make a jet by failing the jet requirements. A NLO calculation of this cross section is under investigation.

6 Properties of multi-jet final states

In previous sections, the QCD theoretical predictions were compared to experimental results in inclusive jet and inclusive di-jet final states and it has been shown that they describe the data very well. We now then ask: Can QCD be as successful in describing multi-jet systems? Only tree level calculations exist describing multi-jet ($N_{jet} > 2$) final states. Is this LO exact calculation accurate enough to describe correlations in multi-jet systems? Is parton shower Monte Carlos which are mostly based on $2 \to 2$ tree level calculation with gluon radiation sufficient in describing multi-jet systems?. Now that the statistics of final state jet events are sufficiently large at the Tevatron, experiments can study multi-jet systems and answer these questions.

The CDF experiment has compared the PQCD predictions on various kinematic quantities and correlations for multi-jet final states. The events are selected requiring a threshold on the scalar sum of E_T in the event greater than 420GeV. To keep the detector acceptance uniform and easily understandable as a function of the invariant mass, an angular cut of $| cos\theta^* | < 0.67$ where θ^* is the polar angle of the leading jet in the N-body center of mass frame, and an invariant mass cut of the final state jets $M > 600\ GeV/c^2$ are required. Finally, an E_T cut of 20 GeV is imposed on each of the jets for the full efficiency of the jet reconstruction algorithm.

The leading jet angular distributions in the N-body rest frame, the inclusive E_T distributions of the jets, and the invariant mass distributions of the N-jet final state are then compared with the following three different QCD predictions:

- Tree level exact matrix element calculation [21] for $2 \to N(< 4)$ process smeared with a Gaussian experimental jet energy resolution function.
- LO $2 \to 2$ parton shower Monte Carlo (HERWIG) [10] together with full simulation of the CDF detector
- An analytical form of Rutherford scattering

Figure 14 shows the normalized angular distribution, $cos\theta^*$ where θ^* is the polar angle in the N-jet CMS, of the leading E_T jet for different jet multiplicities. Solid circles indicate the

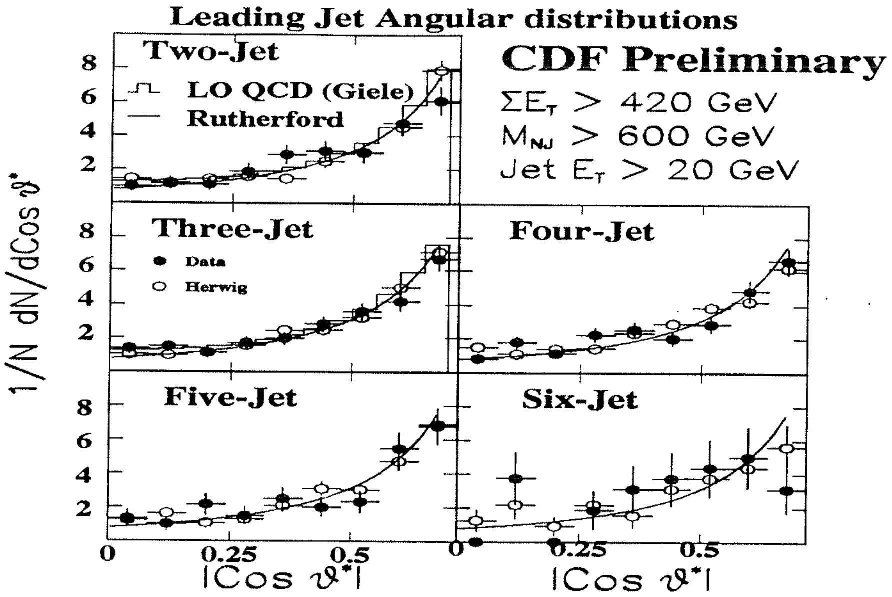

Figure 14: Leading jet angular distributions from CDF up to exclusive six jet events. The distribution is normalized to the total number of events. Solid circles are the experimental measurement. The open circles are parton shower Monte Carlo. The histograms are exact tree level matrix element calculations. The solid lines are the simple analytical form of Rutherford scattering angular distribution.

experimental data, the histograms indicate exact tree level matrix element calculations, solid lines represent the simple analytical form of Rutherford scattering angular distribution, and the open circles indicate parton shower Monte Carlo. The leading jet angular distributions show the same general shape as inclusive di-jet distributions in Fig. 6. In addition, the angular distributions do not vary very much with the jet multiplicity. Comparisons of the data with three theoretical predictions show that all three predictions can describe the shape of the leading jet angular distribution very well independent of the jet multiplicity. Hence, we can draw a conclusion that the leading jet angular distribution is less sensitive to the topology of the event and LO predictions can sufficiently describe the distribution independent of the jet multiplicity in the region of $cos\theta^*$ tested.

Figure 15 demonstrates the inclusive jet P_T spectrum of the multi-jet final states normalized to the total number of events. The solid circles indicate data, the histograms are the parton shower Monte Carlo predictions, and the solid lines represent exact tree level matrix element calculation. The theoretical predictions include all the detector effects such as trigger efficiency and jet energy resolutions. The shape of the distribution is well described by the tree level exact matrix element calculation up to three jet final states where the calculation exist. On the other hand, HERWIG Monte Carlo prediction can describe the shape up to seven jet final state and the agreement is remarkable considering the fact that the prediction is only based on the $2 \rightarrow 2$ tree level calculation with gluon radiation.

Figure 16 shows invariant mass distributions of the multi-jet system normalized to the total number of events. Solid circles represent data, solid lines indicate exact matrix element

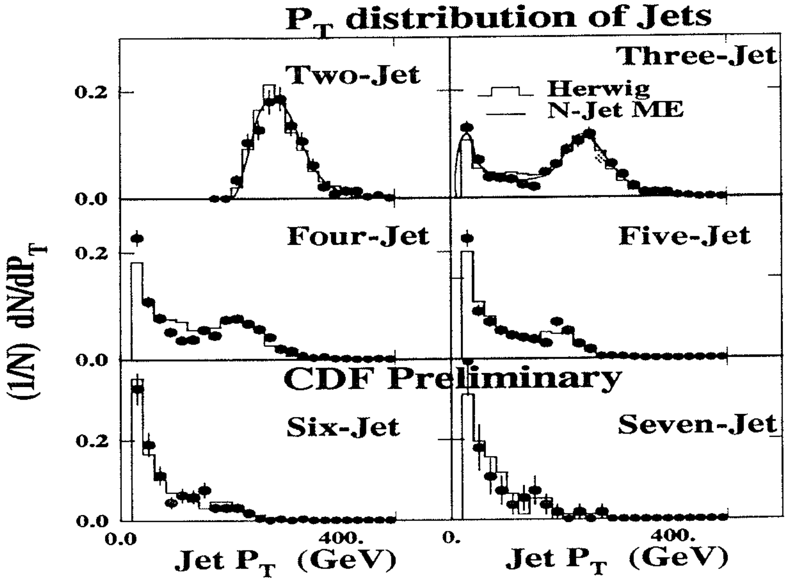

Figure 15: Inclusive E_T distributions of jets from CDF for different multiplicities. The distribution is normalized to the total number of events. The solid circles are the data. The histograms indicate the QCD predictions from HERWIG. The solid lines represent exact tree level calculation.

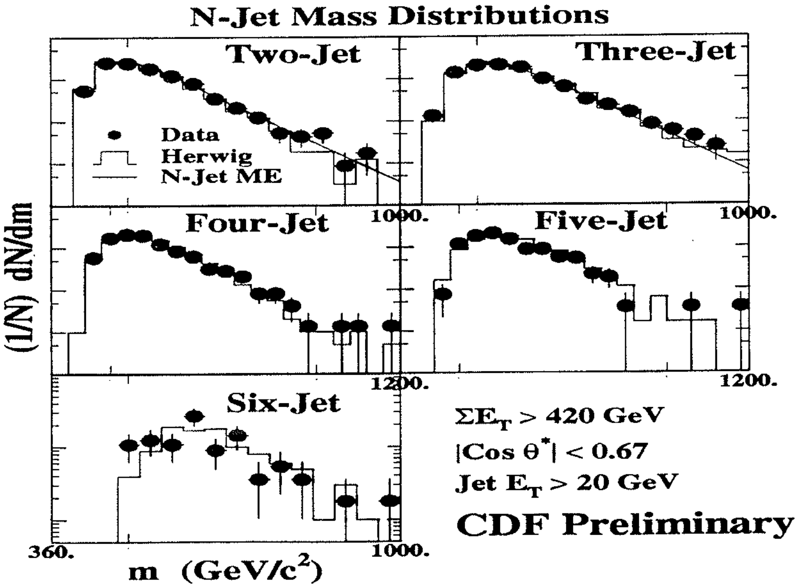

Figure 16: Invariant mass distributions of the N_{jet} final state from CDF for different jet multiplicities. Solid circles indicate the experimental data. The histograms represent HERWIG prediction. The solid lines are exact tree level matrix element calculation.

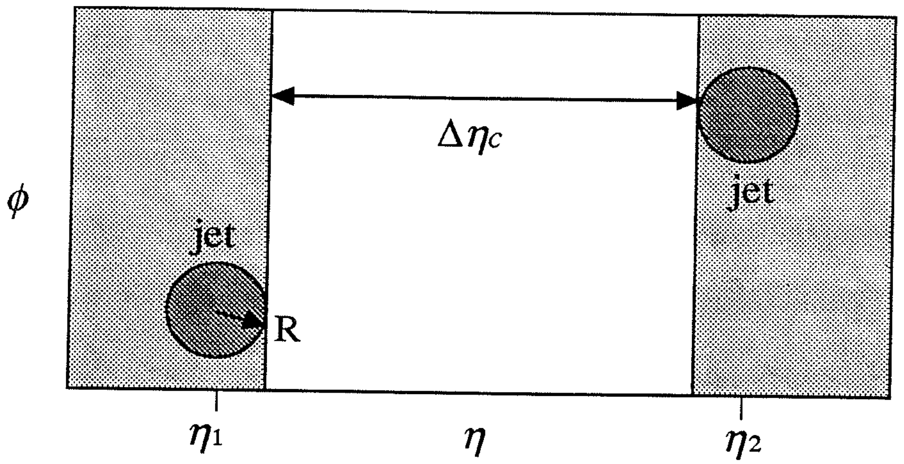

Figure 17: Representation of particle distributions in $\eta - \phi$ space in a typical event with a rapidity gap. The rapidity region between the edges of the jet cones with a radius R, $\Delta\eta_c = \mid \eta_1 - \eta_2 \mid -2R$, contains no particles.

calculation in LO, and the histograms represent HERWIG MC predictions. The trigger threshold effect on the distribution can be observed at lower mass bins near the threshold on the scalar E_T (420 GeV). Again the shape of the distribution to three jet events are well described by the exact matrix element calculation. In addition, the HERWIG Monte Carlo with its radiation can describe the shape well for final states containing up to six jets.

The studies of various measurables in multi-jet final state show that the LO predictions, whether they are tree level matrix element calculations or parton shower Monte Carlo, describe the shapes of the distributions well. We know that LO prediction reaches its limit in describing some correlations (see for example section 5), however, it will be interesting to investigate other observables in the future.

7 Rapidity gap measurements

Rapidity gaps, which are regions in rapidity with no particles, have typically been associated with low momentum transfer processes such as elastic and diffractive scattering. However, it is also expected to occur in high momentum transfer processes when a color singlet particle is exchanged between hard scattering initial state partons [22, 23]. These gaps occur between the final state jets due to the absence of radiation from the color singlet mediator. Hadrons are produced only between the final state jets and the beam direction, leaving the rapidity space between the two jets free of particles. Figure 17 shows an example of an event topology with rapidity gap between two final state jets. $\Delta\eta_c$ is the pseudorapidity separation between the edges of the jet cones, $\Delta\eta_c = \mid \eta_1 - \eta_2 \mid -2R$. This event topology can be observed in the following few cases:

- when a photon, W, or Z is exchanged.
- when a hard Pomeron, which has been shown to be associated with jet production [24] and is also a color singlet, is exchanged.
- Fluctuations in particle multiplicity between jets in a color octet exchange.

However, if the spectator interactions - the interactions between the partons not participating the hard scattering - produce particles between final state jets, the rapidity gaps will not be preserved. While the theoretical interest in this measurement is the actual cross section of the rapidity gap from the hard scattering (σ_{gap}) and the probability of the gap events surviving the spectator interactions (S), the experiments are only sensitive to the product of these quantities. The product of these quantities is called rapidity gap fraction and is defined as:

$$f(\Delta\eta_c) = \frac{\sigma_{gap}(\Delta\eta_c) \cdot S(\Delta\eta_c)}{\sigma(\Delta\eta_c)} \tag{6}$$

Figure 18 shows a naive schematic view of the behavior of the gap fraction for different processes. Since the gaps can occur in color octet exchange from the fluctuations of particle multiplicity, the gap fraction will follow a Poisson statistics and decay roughly like $e^{-\Delta\eta_c}$. The gap fraction from color octet exchange is demonstrated in Figure 18.a. On the other hand, the gap fraction for color singlet exchange is independent of $\Delta\eta_c$, providing a constant level of the fraction as illustrated in Fig 18.b. Since experimentally the gap fractions from these two processes are undistinguishable, however, only the sum of these two gap processes can be observed. Therefore, the experimentally gap fraction will look like Fig 18.c.

Although the theoretical definition of $\Delta\eta_c$ is an empty space in rapidity without any particle contamination, it is very difficult to have the same definition experimentally because counting individual particles particularly at low energy with full efficiency in the detector is impossible. Therefore the DØ experiment has chosen an experimentally achievable definition of the gap by requiring no electromagnetic calorimeter tower with transverse energy greater than 200MeV in rapidity space between the two jets. This definition is 95% efficient in rejecting electromagnetically interacting particles with 2GeV and 40% efficient for hadronic particles with 2 GeV. Figures 19 and 20 show the measured gap fraction, based on the above experimental definition of the gap, as a function of $\Delta\eta_c$ for CDF and DØ experiment, respectively. The fractions show the behavior as naively expected in Fig 18. The fraction decreases exponentially to $\Delta\eta_c \sim 1.0$ and levels out as $\Delta\eta_c$ increases.

While a direct measurement of the fraction, $f(\Delta\eta_c)$, is difficult due to the inherent inefficiency of the detectors in detecting low energy particles, it is possible to determine an upper limit of the fraction using the experimental definition mentioned above. Since the measured gap fraction includes both color singlet and color octet contributions, an upper limit on the gap fraction provides a conservative upper limit on the magnitude of color singlet exchange. The measured gap fraction from the DØ experiment in Fig. 20 is determined to be $f(\Delta\eta_c > 3)^{exp} = (5.3 \pm 0.7(stat) \pm 0.6(sys) \times 10^{-3})$ where only events with $\Delta\eta_c > 3$ are used so that the contribution from color octet exchange is minimized. The systematic error includes a 7% uncertainty from the jet energy scale, and 5% from efficiency and other detector effects

Components of the gap fraction

(Naive expectation of $f(\Delta\eta_c)$ from Bjorken)

Gap process	Behavior of $f(\Delta\eta_c)$
Color octet (parton) exchange - gaps from fluctuations	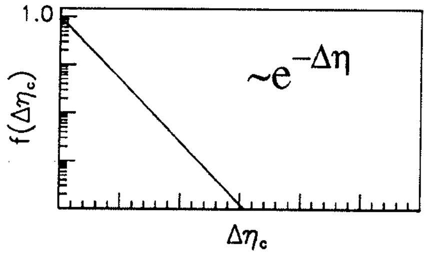
Color singlet exchange	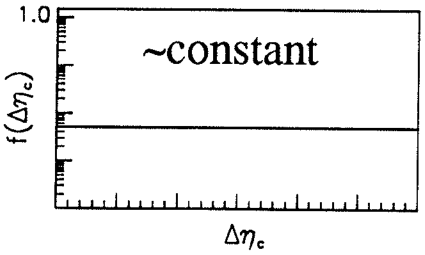
Inclusive gap production	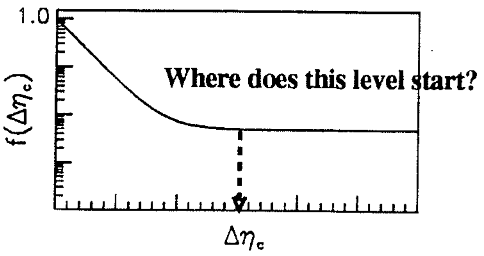

Figure 18: Naive expectations of behavior of the gap fraction, $f(\Delta\eta_c)$ for: a. color octet exchange, b. color singlet exchange, and c. sum of the two processes as experimentally measured.

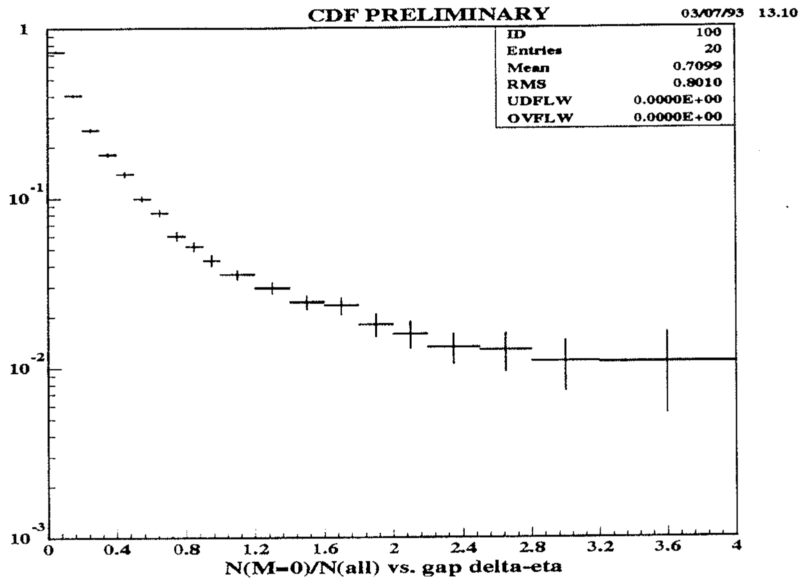

Figure 19: Rapidity gap fraction measured in the CDF experiment.

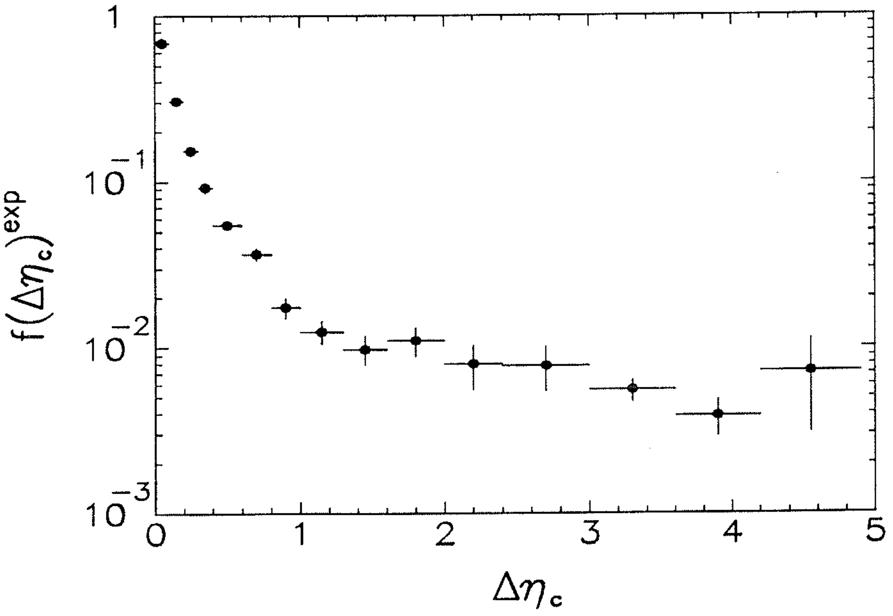

Figure 20: Rapidity gap fraction measured in the D0 experiment

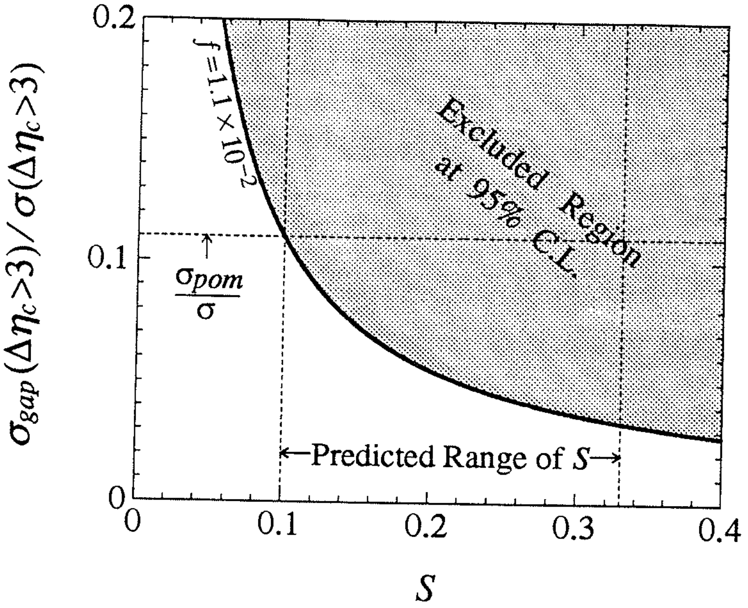

Figure 21: Limit on rapidity gap events from DØ experiment [25]

as well as multiple interactions. It is also found that the secondary particles that shower outside of jet cone can reduce the gap fraction by depositing energy into calorimeter cells around the jets. Therefore it is necessary to correct for this effect before one can place an upper limit on the fraction. This effect reduces the multiplicity of events with $\Delta\eta_c > 3$ by approximately $(35 \pm 5)\%$. After the correction the upper limit on $f(\Delta\eta_c > 3)$ is

$$f(\Delta\eta_c > 3) < 1.1 \times 10^{-2} \tag{7}$$

at 95% confidence level. Figure 21 shows excluded regions of σ_{gap}/σ and S space for $\Delta\eta_c > 3$. The two dotted vertical lines indicate the theoretically predicted range of the survival probability and the dotted horizontal line indicate an estimate of the true gap fraction by Bjorken from the contribution of a Pomeron exchange. The shaded region represents the excluded region of the true gap fraction and the survival probability by the upper limit in Eq. 7. As one can see, that a large fraction of theoretically allowed region is excluded.

8 Direct photon inclusive P_T spectrum

Events with high P_T isolated photons provide a good laboratory for studying high momentum transfer phenomena. Since photons are electromagnetically interacting particles, this process has less uncertainties from non-perturbative effects, such as fragmentation and hadronization, compared to jet final states. Because of this, it is an ideal final state to be compared to QCD predictions. In addition, the direct photon process at the Tevatron is dominated by the gluon Compton process. Therefore, understanding this spectrum can provide important gluon parton distribution function information. Now that the NLO prediction [26] of this process is available, the theoretical predictions of the cross section is more stable, and the comparison between experimental data and the theoretical prediction becomes more reliable.

The biggest difficulty in this measurement resides in background estimation. Since the final state of direct photon process consists of an isolated photon balanced by a hadronic jet, single neutral particles that decay immediately to multi photons, such as π^0 or η^0, from fluctuations of jets in QCD di-jet events are the dominant sources of backgrounds. To estimate the background contamination from these multi-photon sources, a shower profile method and conversion methods are commonly used. Since, the opening angle between multi photons from neutral hadron decay becomes large at low parent momentum, the difference of the shower profile from the single photon and from multi-photon induced showers can be used to distinguish backgrounds from direct photons. However, the systematic uncertainty of this method grows fast as the parent momentum increases because the opening angle of the multi-photon becomes smaller. Therefore, a conversion method is used to complement the shower profile method at higher photon momentum. The conversion method uses the fact that the conversion probability of n photons traversing collinearly in material is n times bigger than that of a single photon.

To estimate the background fraction, the CDF detector utilizes CPR (Central Preshower detector) and CES (Central Electromagnetic Strip chamber). The CES provides accurate measurement of shower profile at the shower maximum of an electromagnetic shower and is used for shower profile background estimation. On the other hand, the CPR provides accurate counts of photon candidates converted before and after the detector and is used for background estimation at high P_T. The D0 experiment at this point uses the conversion method to estimate the background by counting the conversions of photon candidates in the tracking system. The conversion method using the first layer of electromagnetic calorimeter which provides approximately 2 radiation length of material is also under study.

Figure 22 shows the central, $|\eta| < 0.9$, inclusive photon cross section, $d\sigma^2/dP_T d\eta$, after background subtraction from the CDF experiment. The solid triangles indicate experimental data with error bars indicating statistical uncertainty only. The typical normalization uncertainty from luminosity measurement is illustrated on the plot. The solid line indicates a NLO QCD prediction using CTEQ1M parton distribution functions with renormalization scale, $\mu_R = P_T/2$ whereas the dashed line represents the same prediction with $\mu_R = 2P_T$. The systematic uncertainty from background estimation is demonstrated in Fig. 24.b as a function of photon P_T. One can observe the fast increase in systematic error as the photon P_T decreases. The typical size of the uncertainty varies between 60% and 15% depending on the photon P_T. Figure 23 shows the same cross section from the D0 experiment. Various symbols indicate experimental data for different overlapping triggers to cover different ranges of photon P_T. The inner error bars represent the statistical uncertainty and the outer error bars indicate systematic uncertainties. The dominant systematic uncertainty comes from background estimation which typically runs between 50% to 30% depending on photon P_T. The solid line indicates NLO QCD prediction using CTEQ1M parton distribution functions with $\mu_R = P_T$. The cross sections span several orders of magnitude and show good agreement with the NLO theoretical prediction in a wide range of photon P_T. Especially, the agreement in high P_T is remarkable. However, the CDF experiment observes disagreement

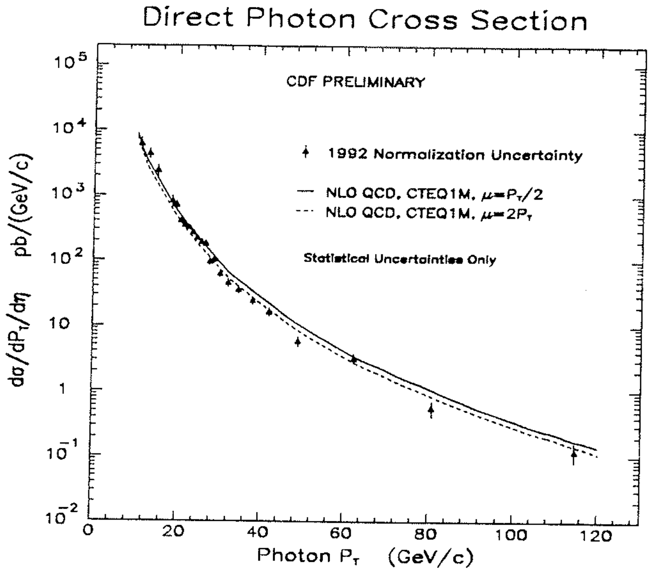

Figure 22: Inclusive P_T spectrum of photons in the central rapidity region, $\mid \eta \mid < 0.9$, from CDF experiment. The solid triangles represent experimental data. The error bars on each data point represent statistical uncertainties only. The solid and dashed line indicate NLO QCD prediction using CTEQ1M parton distribution function with renormalization scale, $\mu_R = P_T/2$ and $\mu_R = P_T$, respectively.

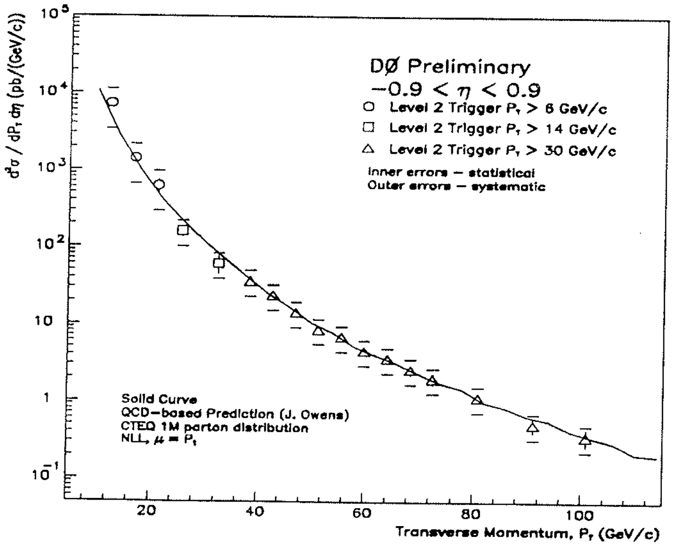

Figure 23: Inclusive P_T spectrum of photons in the central rapidity region, $\mid \eta \mid < 0.9$, from the D0 experiment. Different symbols represent experimental data from different triggers which cover a wide range of photon P_T. The inner error bars indicate statistical uncertainty and the outer error bars indicate the statistical uncertainty. The solid line illustrates NLO theoretical prediction using CTEQ1M with $\mu_R = P_T$.

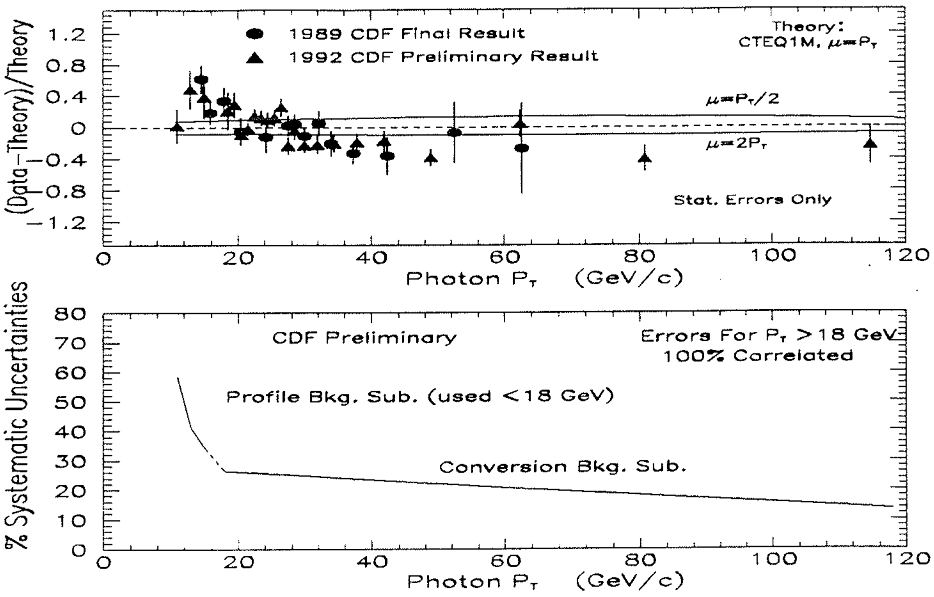

Figure 24: a. Difference between theoretical prediction and the data divided by the theoretical prediction. The prediction used CTEQ1M PDF with $\mu_R = P_T$. Two solid lines represent NLO theoretical predictions with two different μ_R.
b. Systematic error from various background estimation method as a function of photon P_T from CDF

between data and the prediction at lower P_T. Figure 24.a shows the difference between NLO theoretical prediction with the CTEQ1M parton distribution functions and the data normalized to the theoretical prediction as a function of photon P_T to illustrate this difference. The solid circles represent the CDF results from the 1989 data analysis whereas the solid triangles indicate the 1992 data. One can observe a systematic increase of the ratio as photon P_T decreases below 20 GeV. The two solid lines show the same ratio between theoretical predictions with different renormalization scale ($\mu_R = P_T/2$ and $\mu_R = 2P_T$). The change of renormalization scale is only in the absolute normalization in the cross section, but not in the overall shape of the distribution.

The low P_T spectrum of the photons is dominated by gluon Compton process and gluon distribution is not directly measurable by other deep inelastic experiments. So the large uncertainty in the gluon distribution could cause the difference between the theoretical prediction and the experimental data. This discrepancy is under investigation in great detail by the CDF experiment. One of the best ways to achieve better information on the gluon parton distribution function is the measurement of the inclusive photon cross section as a function of rapidity out at high rapidity($\eta > 2.0$) [28].

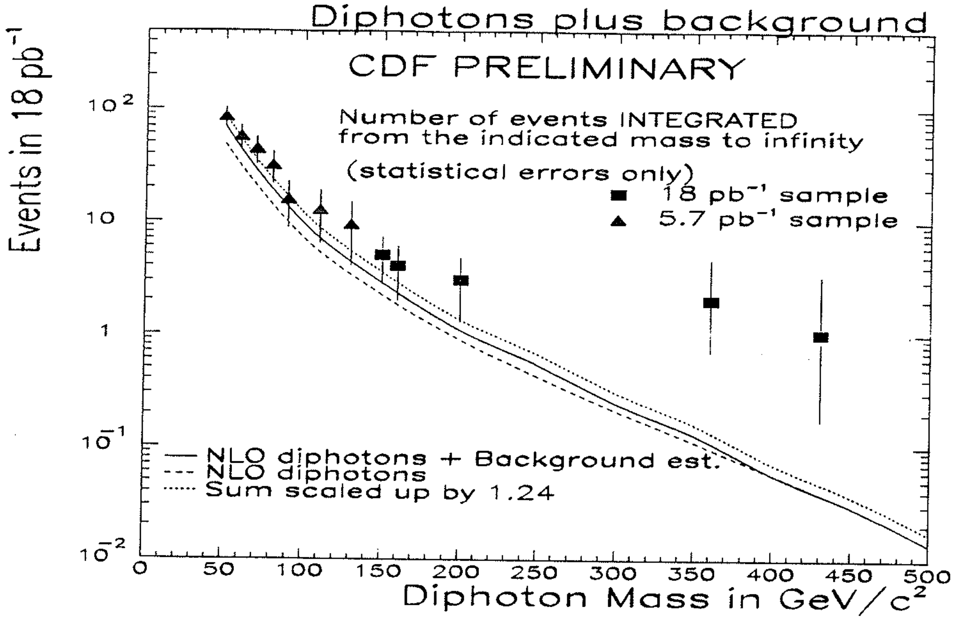

Figure 25: Integrated invariant mass distribution of two photons events from CDF experiment.

9 Two photon cross sections

The two photon final state has three dominant Feynmann diagrams: the quark-antiquark annihilation diagrams ($q\bar{q} \rightarrow \gamma\gamma$), the fermion box diagrams ($gg \rightarrow \gamma\gamma$), and bremsstrahlung diagrams (e.g., $qg \rightarrow \gamma\gamma q$). This process is one of the dominant background processes for Higgs bosons in the intermediate mass range which decay to two photon final state. Therefore, understanding this process is very important for future Higgs searches in higher energy colliders, such as the LHC.

To study the characteristics of the two photon final state, CDF has measured the invariant mass distribution of two photon final state events. Figure 25 illustrates the integrated invariant mass distributions of the two photons in the final states. The solid line indicates the NLO theoretical prediction with background included. The dashed line represents the NLO predictions [29] without background. The dotted line indicates the NLO prediction including background scaled up by factor 1.24. The solid triangles represent the data of the part of the 1992 run ($5.7pb^{-1}$) from a trigger and the solid squares indicate the data from a different trigger. With the given statistics from the 1992 run, the CDF experiment extended the invariant mass to approximately 500 GeV. As can be seen from Fig. 25, NLO QCD prediction agrees with data the best if it is scaled up by factor 1.24. However, there are two events with two photon mass above 350GeV and these events are currently under investigation.

Figure 26 shows the cross section of two photon plus one jet final state as a function of sum of the scalar E_T of the objects in the event. The solid line indicates the NLO theoretical prediction with background and the dotted line illustrates the same prediction

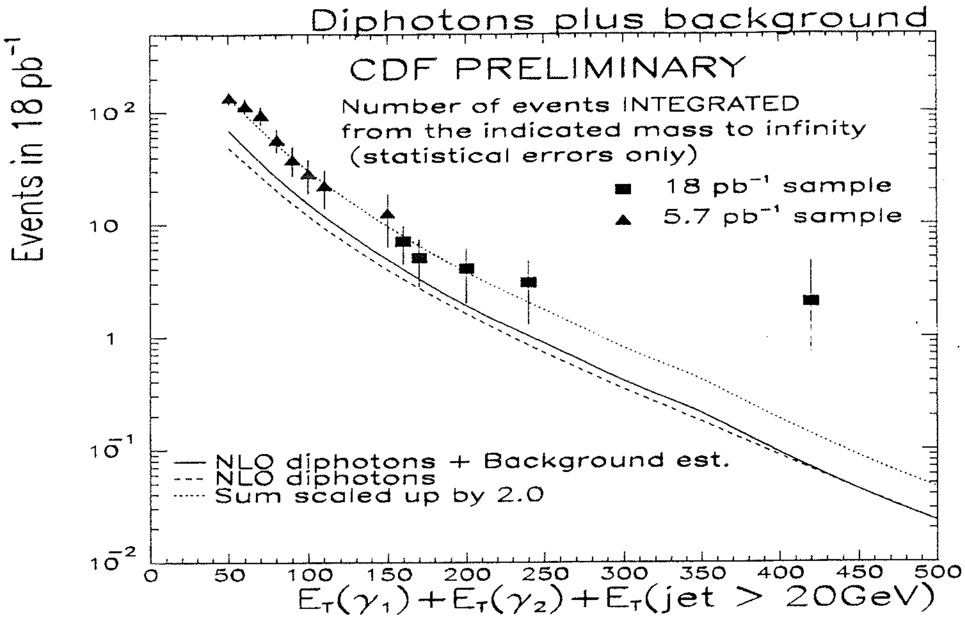

Figure 26: $\Sigma \mid E_T \mid$ distribution of two photon plus one jet final states from CDF experiment

scaled by factor 2. The NLO QCD prediction seems to have a normalization uncertainty in describing the cross sections of two photon final state in various kinematic quantities. The two events with large mass also has large sum E_T of the observed objects. While these events could be an indication of deviation from QCD prediction, it is still too early to draw any conclusion from these events. It is noteworthy, however, to emphasize that Tevatron has started providing windows on these rare events with two photon final state which would be a considerable help in understanding detailed prediction of QCD.

10 Conclusions

In this review, many QCD analyses with jet and direct photon final state at the Fermilab experiments were discussed. Both experiments use their experimental strength to probe the theory in many different aspects and are complementing each other. Parton level predictions of QCD in LO and NLO as well as parton shower Monte Carlo predictions were compared with experimental data in many physical observables.

Theoretical predictions at the parton level are very successful in describing inclusive cross sections such as inclusive jet and photon E_T spectra as well as inclusive di-jet angular distributions. Internal structure of jets are measured and compared both NLO PQCD and parton shower Monte Carlo predictions. The PQCD predictions can describe this structure qualitatively well but still bare normalization uncertainty. The parton shower Monte Carlo describes the structure very successfully. More complex correlations of the di-jet and multi-jet systems were studied. In general, the theoretical predictions describe most correlations well. However, the experimental data for di-jet triple differential cross section disagree with the available theoretical predictions and need higher order calculations.

First result of rapidity gap measurement from the D0 experiment is published in Ref. [25]. Further analyses to measure the cross section for color singlet exchange are in progress at the Tevatron.

High CMS energy of the Tevatron and increased statistics open the door for investigating rare events such as two photon final state. Various kinematic quantities for the two photon final state are compared with available predictions. The current NLO PQCD predictions in describing these quantities bares large normalization uncertainty.

References

[1] D. J. Gross and F. Wilczek, Phys.Rev. **D8**, 3633 (1973).

[2] H. Fritzsch, M Gell-Mann and H. Leutwyler, Phys. Lett. **47B**, 365 (1973)

[3] D. P. Barber *et al*, Phys. Rev. Lett. **43**, 830 (1979);
G. Wolf *et al*, (TASSO collaboration), Lepton/Photon Symp.1979 **34**, QCD161:I71 (1979);
W. Bartel *et al*, (JADE collaboration), Phys. Lett. **91B**, 142 (1980)

[4] E. Barsotti *et al* (CDF collaboration), Nucl. Instr. and Meth. Phys. Res, **A269**, 82 (1988).

[5] S. Abachi *et al* (D0 collaboration), Nucl. Instr. and Meth., **A338**, 185 (1994).

[6] S. Ellis, Z. Kunszt, and D. Soper, Phys. Rev. Lett. **62**, 2188 (1989)

[7] J. Alitti *et al* (UA2 collaboration), Phys. Lett. **B257**, 232 (1991).

[8] D. Amati and G. Veneziano, Phys. Lett. **B83**, 87 (1979);
G. Marchesini, L. Trentadue and G. Veneziano, Nucl. Phys. **B181**, 335 (1981);
Y. I. Azimov, Y. L. Dokshitzer, V. A. Khoze and S. I. Troyan, Z. Phys. **C27**, 65 (1985)

[9] F. Abe *et al* (CDF collaboration), Phys. Rev. Lett. **70**, 713 (1993).

[10] G. Marchesini and B. Webber, Nucl. Phys **B310**, 461 (1988)

[11] S. D. Ellis, Z. Kunszt, and D. E. Soper, Phys. Rev. Lett. **64**, 2121 (1990).

[12] F. Abe *et al.* (CDF collaboration), Phys. Rev. Lett.**70**, 713 (1993).

[13] J. W. Gary, Proceedings of the workshop "QCD at 2 TeV", Michigan State University, East Lansing, MI, USA, Oct. 29-30 (1993).

[14] "The PAPAGENO Partonic Monte Carlo program", I. Hinchliffe, LBL-34372, July 1993

[15] D. W. Duke and J. F. Owens, Phys. Rev. **D30**, 49 (1984).

[16] for NLO, the scale: $M_{jj}/4cosh(0.7\eta^*)$ is used as suggested in [17].

[17] S. Ellis, Z.Kunzst, D.Soper, Phys. Rev. Lett. **69**, 1496 (1992).

[18] F. Abe *et al* (CDF collaboration), Phys. Rev. Lett. **69**, 2896 (1992).

[19] J. G. Morfin and W. K. Tung, Z. Phys. **C52**, 13 (1991).

[20] W.T. Giele, E.W.N. Glover, and David A. Kosower, Nucl. Phys. **B403**, 633 (1993).

[21] F.A. Berends, W.T. Giele, and H. Kuijf, Phys. Lett. **B232**, 266 (1989);
F.A. Berends and H. Kuijf, Nucl. Phys. **B353**, 59 (1991).

[22] Y. Dokshitzer, V. Khoze and S. Troyan, Proceedings of the 6th International Conference on Physics in Collisions (1986), ed. M. Derrick (World Scientific, Singapore, 1987).

[23] J. D. Bjroken, Phys. Rev. **D47**, 101 (1992).

[24] A. Brandt *et al.* (UA8 collaboration), Phys. Lett. **B297**, 417(1992).

[25] S. Abachi *et al.* (D0 Collaboration), Phys. Rev. Lett. **72**, 2332 (1994).

[26] H. Bare, J. Ohnemus, and J. F. Owens, Phys. Lett. **B234**, 127 (1990).

[27] J. Kwiecinski, A. D. Martin, R. G. Roberts, and W. J. Stirling, Phys. Rev. **D 42**, 3545 (1990).

[28] P. Aurenche *et al*, "Physics at Fermilab in the 1990's", Breckenridge, Colorado, August 15-24 (1989), 212 (eds. D. Green & H. Lubatti).

[29] B.Bailey, J.F.Owens and J.Ohnemus, Phys. Rev. D46, 2018 (1992).